Chapter 10
Realization of Artificial Chirality in Micro-/Nano-Scale Three-Dimensional Plasmonic Structures

Younghwan Yang, Yeseul Kim, Junho Gwak, Sunae So, Jungho Mun, Minkyung Kim, Heonyeong Jeong, Inki Kim, Trevon Badloe, and Junsuk Rho

Abstract Recent advancements in nano- and micro-fabrication technology have allowed the realization of artificial structured materials with strong electromagnetic chirality, far-exceeding natural chiral materials. This chapter categorizes the fabrication methods for realizing chiral structures based on the feature sizes, which closely relates to the operating wavelengths. Conventional top-down and bottom-up approaches are discussed along with their respective advantages and disadvantages, and the recently developed unconventional fabrication methods are also provided. Additionally, the chiral responses of the fabricated structures are briefly introduced. This chapter will contribute to the understanding of possible chiral structure designs and help to develop further fabrication methods for improving chiroptical activity.

10.1 Introduction

A chiral object cannot be superimposed onto its mirror image by only translations and rotations. In general, a chiral object and its mirror image (enantiomer) have identical physical characteristics such as mass, so they cannot be distinguished easily [1]. However, they may interact differently with other chiral objects; this feature has significant implications in pharmaceutics and synthetic chemistry, because a chiral molecule and its enantiomer have different chemical properties. Such chiral objects interact enantioselectively with circularly-polarized light, i.e., the chiral

Y.Yang and Y. Kim have contributed equally to this work.

Y. Yang · Y. Kim · J. Gwak · S. So · M. Kim · H. Jeong · I. Kim · T. Badloe · J. Rho (✉)
Department of Mechanical Engineering, Pohang University of Science and Technology (POSTECH), Pohang 37673, Republic of Korea
e-mail: jsrho@postech.ac.kr

J. Mun · J. Rho
Department of Chemical Engineering, Pohang University of Science and Technology (POSTECH), Pohang 37673, Republic of Korea

© Springer Nature Switzerland AG 2021

E. Kamenetskii (ed.), *Chirality, Magnetism and Magnetoelectricity*,
Topics in Applied Physics 138,
https://doi.org/10.1007/978-3-030-62844-4_10

objects interact differently with left-circularly-polarized (LCP) and right-circularly-polarized (RCP) light. Their absorption difference under LCP and RCP incidences is circular dichroism (CD), and the polarization rotation of light interacting with the chiral objects is optical rotatory dispersion. However, naturally occurring materials have intrinsically weak chiroptical responses, or circular birefringence, due to the large mismatch between the wavelength and the sizes of chiral molecules. This weak response hinders application of chiroptical properties.

Recent advances in artificial chirality in structured materials suggest a possibility of generating materials that have strong chiroptical properties that far exceed those found in natural materials, and chiral effects have been observed universally across different length scales. According to the antenna theory [2], the resonant wavelength of a single antenna is comparable to its geometric feature size. This principle also applies to chiral effects; the working wavelength of the chiral effects becomes generally similar to the geometric feature size of the chiral antenna. Therefore, chiral antennas that operate at wavelengths of micrometers or longer are relatively easy to fabricate. This principle applies because the optical properties of metals at long wavelengths are well represented as conductor (metallic) [3]. However, the optical properties of metals near the plasma frequency become strongly dispersive and deviate from those of a perfect conductor. Due to this feature, metallic antennas become lossy at wavelengths near the visible regime. With these points in mind, fabrication methods should be considered with regards to the desired working wavelength and the properties of the material.

Recently, subwavelength metallic particles have been actively investigated for surface-enhanced Raman scattering [4], photothermal effects [5], and optical antennas [6] due to their strong near-field enhancement and scattering effects, which originate from localized surface plasmon resonance (LSPR) coming the collective oscillations of electrons and photons trapped on the surface of the small particles [7]. When the particle size is much smaller than the wavelength, the LSPR can be predicted using the quasistatic theory. Therefore, the metallic antennas near the visible regime are distinguished from those at longer wavelengths as plasmonic antennas. The wavelength scaling principle above does not apply to plasmonic antennas [3], and subwavelength (~10 nm) chiral plasmonic nanoparticles (NPs) have strong chiral effects in the visible spectrum. In addition, the LSPR wavelength can be further redshifted without increasing the particle size by using high refractive index core and plasmonic shell [8, 9].

In this chapter, we discuss a few fabrication methods of chiral structures and their applications. Sections are divided according to the structure size, because it determines working wavelengths and the fabrication methods, and applications strongly depend on the working wavelengths.

10.2 Chirality at the Micrometer-Scale or Higher: Top-Down Approach

This chapter will introduce chiral plasmonic structures and their realization in micrometer-scale or beyond by using top-down fabrication. Artificial microscale structures generally interact with electromagnetic (EM) waves of 1 μm or more. The wavelength range ($\lambda > 1.0$ μm) includes infrared and microwave regions; they can be utilized for thermal detectors, light detection and ranging (LiDAR) devices, short-range wireless communication antenna, and spectroscopy. With these applications in mind, chiral plasmonic structures have been demonstrated from 1 μm size structures to millimeter-scale chiral ones. In this subchapter, their fabrication methods will be categorized by scales of artificial structures sizes; brief descriptions of chiroptical phenomena will be added.

10.2.1 Direct Laser Writing

A few micrometer-scale chiral structures (e.g. helical structures) have been fabricated using direct laser writing (DLW). This method can yield structures that have high aspect ratio, and that demonstrate a multi-pitch helix (Fig. 10.1a–c). These structures exhibit different chiroptical properties depending on how their helicities are designed. For example, two-pitch helical structures have been investigated as metamaterials to induce broadband, strong CD (Fig. 10.1a) [10]. In the wavelength range $3 \leq \lambda \leq 6.5$ μm, chiral structures interact only with EM waves that have the same handedness of polarization.

The corresponding structures are fabricated (Fig. 10.1d) by combining DLW and electroplating with a positive-tone photoresist (PR). First, a substrate coated with

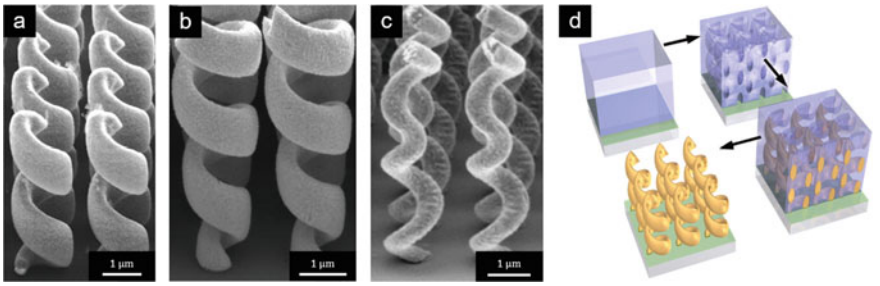

Fig. 10.1 SEM images and schematic of fabrication methods with direct laser writing. This method can fabricate **a** multi-pitch gold helixes, **b** tapered helixes and **c** handedness-converted helical structures. **d** The illustration shows fabrication process of gold helixes by combining direct laser writing and electroplating process. A positive photoresist is spun onto a substrate. And then, patterns are exposed by direct laser writing. Vacancies are filled with gold with electroplating. Gold structures are finally fabricated with removing the residual photoresist. (**a**) and (**d**) from [10], (**b**) from [11], (**c**) from [12]

thin indium-tin-oxide (ITO) is prepared, and then a positive-tone PR is spin-coated on it. The ITO has electrical conductivity, which is required to allow use of the electroplating processes. Second, the positive-tone PR is polymerized using focused photons, and the exposed spot is removed after the development process. Third, electrochemical deposition is conducted to grow gold structures in the voids in the polymer. Gold is a typical material for chiral plasmonics due to its high conductivity to enable electron oscillations, and to its resistance to corrosion. Finally, the remaining PR is removed using oxygen plasma etching to leave sophisticated gold structures.

The main strength of DLW is that three-dimensional printing induced by multi-photon polymerization yields the highest degree of design freedom [13, 14]. DLW can fabricate various helical structures, which have different chiroptical activities depending on the helical parameters and design. For example, tapered helical structures [11] increase extinction ratio and broaden bandwidth simultaneously. Handedness-converted helical structures achieve spin-conversion efficiency within the frequency range of 50−90 THz ($6 \geq \lambda \geq 3.33$ μm) (Fig. 1d) [12]. However, DLW has the disadvantage of limited resolution, so the wavelength band in which it works has a lower limit. The method is also slow, so it cannot be used practically to pattern large areas.

10.2.2 Buckling Process Using Focused Ion Beam

Thin-film buckling process enables curved surfaces with sizes of tens of micrometers; the curvature enables three-dimensional chiral structures. This thin-film-buckling method includes cutting and folding flat objects. Some three-dimensional chiral structures have gigantic chiral phenomena, compared to two-dimensional chiral structures [15]. Furthermore, this buckling process does not require stacking and aligning, which are necessary steps in multi-layer fabrications. The residual stress can be induced by various stimuli, including temperature, mechanical forces, and capillary forces [16–19]. In this subchapter, we will consider focused ion beam (FIB)-induced buckling which is a recently emerging method.

Residual induced compressive forces have been evaluated as methods to create chiral structures and strengthen their chiroptical responses [20]. One method to generate residual stress in a surface of thin film is to use FIB to implant ions. This technique requires only a single step, and has both high accuracy and high resolution, so the method can fabricate desirable chiral structures. For example [15], one chiral structure that had a strengthened chiroptical response (Fig. 10.2a); to generate plasmonic responses, the authors used a gold thin film in which residual stress was imposed by global ion beam irradiation (Fig. 10.2b). Curvatures of the structures can be modulated by controlling the dose intensity during irradiation, so chiral structures can be shaped with quite high accuracy (Fig. 10.2c).

Compared to two-dimensional structures, buckled chiral techniques enable versatile geometries. Chirality is derived from the difference in interaction depending

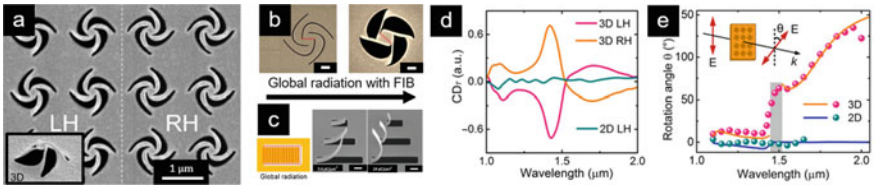

Fig. 10.2 Understanding of buckled structures fabricated by focused ion beam, **a** The rosette arrays are fabricated with buckling process with focused ion beam. Two different handedness can be fabricated, **b** A global radiation buckle a thin films. Right image shows a pre-buckled structure. the left-one shows post-bucked structures, **c** A film are buckled by global radiation, **d** measured chiral reponses of bucked structures, **e** The buckling process dramatically increase an optical rotation. (**a**–**e**) from [15]

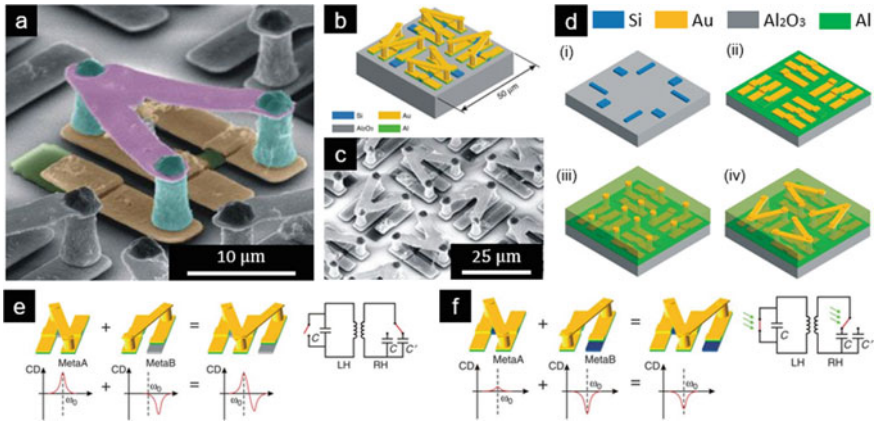

Fig. 10.3 Artificial chiral structures using photolithography and electroplating. **a** SEM image shows fabricated 3D chiral structures, **b** A unit-cell is consist of four-chiral structures and they are composed of four different materials, **c** SEM image shows a rotating arrangement of chiral structures by consisting unit-cell. The rotating arrangement induces chiral responses, **d** Schematic shows a fabrication process for chiral structures, **e**-**f** Handedness switch can be described by LC-circuit interpretation. (**a**–**f**) from [21]

on the spin-states of the circularly-polarized light and can be expanded to three-dimensional twisted structures. The different optical response is related to the electromagnetic coupling, which can be enhanced by three-dimensional structures [22]. Figure 10.2a, b show twisted chiral structures fabricated using a FIB, achieving a strong chiral response from three-dimensional structures using the residual stress of films. This method can be used to create versatile geometric structures with ion beam dose splitting (Fig. 10.2c). The fabricated buckled structures have CD of ~0.5 at 1.45 μm that can be used in telecommunications (Fig. 10.2d). Buckled structures have increased angles of optical rotation, compared to unbuckled structures in the telecommunications region (Fig. 10.2e). These results imply that three-dimensional fabrication methods can strengthen chiroptical phenomena.

Chiral structures with sizes of 10–100 μm have been realized by combining photolithography and electroplating methods. In the terahertz frequency range, silicon can be used as the photoactive materials, and artificial silicon meta-atoms may be described using inductor-capacitor (LC) circuits.

A device that had the above characteristics achieved active metasurfaces that could switch the their handedness [21] (Fig. 10.3a–c); consisted of meta-atoms composed of gold, silicon, aluminum oxide, and aluminum components that had been fabricated using a combination of photolithography and electroplating. To fabricate photoactive chiral metamaterials, firstly, a patterned silicon layer was deposited using photolithography and reactive ion etching. Then aluminum was deposited by sputtering. The aluminum was a conductive layer for electroplating, as the ITO layer, which used in DLW. Sputtering was used due to its high step-coverage. Gold layers were also deposited using photolithography with aligning processes. Gold columns were fabricated using photolithography to exposure photoresist (PR) and electroplating to infill vacancies. This process is similar to DLW with electroplating, but photolithography is more suitable than DLW to fabricate large-area metasurfaces. Finally, the residual resist was removed using oxygen plasma etching, and the aluminum also removed using aluminum etchant. Oxygen plasma etching is a common method to remove PR in complex structures and it can be applied to other processes (e.g. removing PR when helical structures are fabricated using DLW).

These chiral structures can switch the handedness of circularly-polarized light without geometrical reconfiguration. The handedness modulation is achieved by photoactive material and well-designed LC circuits (Fig. 10.3e–f). Gold acts as an ideal conductor, and loops of gold respond as inductors. The gaps between bottom gold plates function as capacitors, so the meta-atom has a resonance frequency like an LC (Fig. 10.3e, MetaA). The short length of MetaB causes a resonant shift, which leads to the chiral response of the meta-atom. The total atom can be interpreted as fusion of a right-handed meta-atom and frequency-shifted left-handed meta-atom (Fig. 10.3e). When photoexcitation of silicon is induced by near-infrared laser pulses, electrons jump from the silicon pad to the conduction bands, so the silicon becomes conductive. This change cancels the capacitance of MetaA, and including frequency shifting of MetaB. As a result, the handedness of chirality is switched by photoactive material property of Si and combination of fabrication methods (Fig. 10.3f).

10.3 Chirality at the Nanometer to Micrometer Scale

10.3.1 Electron Beam Lithography Overlay

The chiral behaviors in a chiral molecule can be explained by movements of electron clouds. Under illumination by circularly-polarized light, electron clouds of the molecules are displaced; this change induces a magnetic moment. It has components that are parallel to the electric dipole moment, and the interaction between

these moments yields the chiral behaviors. This conceptual explanation of chiral behaviors can be transferred to plasmonic molecules. In plasmonic chiral systems, displacement currents are excited inside the plasmonic particles, where free electrons are displaced. Accordingly, a strong chiral response can occur, especially when the currents are accompanied by a resonant excitation of localized plasmons. One way to realize plasmonic chiral molecules is to arrange plasmonic structures in a 'handed' way [21]. One straightforward method to realize such handed structures is to use conventional electron beam lithography (EBL) techniques with a precise overlay process. An accurate EBL overlay method that has sub-20 nm alignment accuracy has been used to realize three-dimensional chiral structures on scales of a few nanometers by stacking plasmonic structures layer-by-layer.

To realize sub-20-nm alignment accuracy, a precise patterning of well-designed alignment mark is necessary. However, the EBL alignment process cannot be seen directly, even using scanning electron microscope. Instead, the relative position of a stage can be predicted by using a set of alignment marks. Therefore, precise alignment marks with sharp corners must be fabricated for use as reference points. Furthermore, by defining alignment marks first, then using them at the beginning of fabrication of the first layer, the alignment accuracy can be improved further. Stage movement is almost identical for a given substrate, so the relative position of first layer and second layer should be affected only by the alignment process. This EBL-overlay process can be used to fabricate many different configurations of 3D nanostructures, such as 3D suspended/connected, interlayered and hierarchical [23]. Artificial chiral structures composed of mirror-symmetric suspended and connected nanostructures show strong chirality at near-infrared (NIR) wavelengths of around 2.1–2.5 μm [23]. The structure has a chiral resonator, in which gold structures form an artificial LC circuit. A tilted metallic loop and the gap effectively function as EM circuit components of an inductor and a capacitor, respectively. Inside the LC circuit, the electric and magnetic dipoles are excited simultaneously because they share the same structural resonances. As a result, the structures can exhibit strong chiral response under the same structural resonances. The structures may exhibit negative refraction if the induced chirality is strong.

The similar idea an also be applied to design planarized chiral helical structures [24]. Metasurfaces are sequentially stacked with a tailored rotational twist that forms anisotropic arrays (Fig. 10.4). The structural anisotropy is effectively converted to strong magneto-electric coupling, which is responsible for artificial chirality. The twisted metasurface structure provides strong coupling between each pair of spaced surfaces over a broad range. If the number of stack sequential layers is increased, the bandwidth broadens, and the reflections of opposite waves increases.

Recently, the concept of chiral molecules to plasmonic structures has been transferred to realize effective chiral molecular structures using a precise EBL overlay. In [25], four gold nano-disks are closely arranged in a handed fashion to form a plasmonic oligomer (Fig. 10.5). The first three particles are placed in the first layer to make an L-shape, and the fourth particle is located in the second layer. The handedness is determined by the location of the last gold particle in the second layer, and the structure exhibits configurational chirality. In this construction rule, the ligands

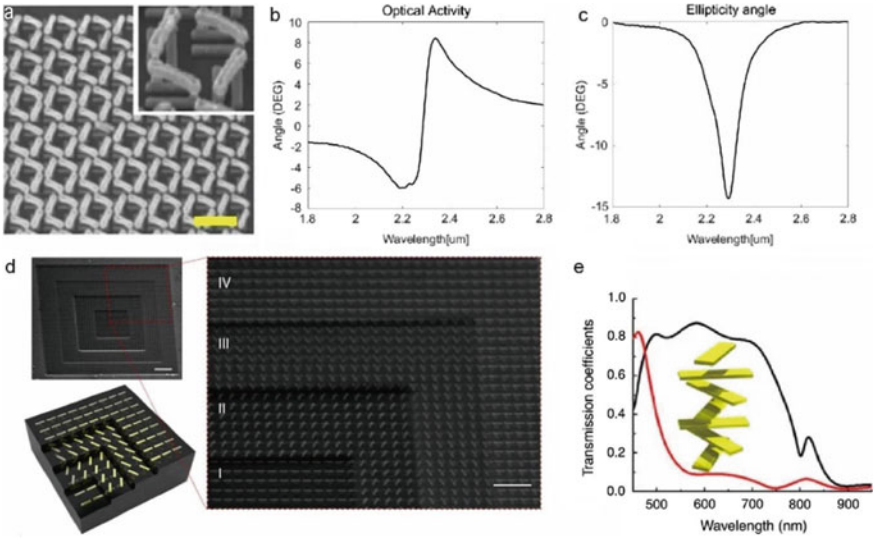

Fig. 10.4 **a** SEM image of the hierarchical, interlayered 3D nanostructure with misalignment kept below 20 nm. The scale bar indicates 500 nm. **b**–**c** Optical activity and ellipticity angle calculated from artificial chirality simulation at NIR frequencies. **d** SEM images of the twisted metamaterial multilayer, where each layer is revealed using FIB to show the corresponding layer of nanorods. **e** Transmission of left and right-handed circularly polarized light through seven layers of twisted nanoslab along the direction of propagation. (**a**–**c**) from [23], (**d**–**e**) from [24]

in chiral molecules can be represented by aligning the metal particles. However, this study showed that the structural handedness is not sufficient to generate a strong chiral response. Resonant plasmonic coupling is also an important prerequisite but can only be accompanied by the interactions of particles with similar resonance wavelengths. Therefore, due to weak coupling, the structures consisting of different size of particles did not show a strong chiral response, despite their geometrical handedness (Fig. 10.5).

The idea of transferring the concept of chiral molecules to plasmonic structures have been extended to the more-complex chiral structures of diastereomers [27, 28]. Diastereomers are two molecules are not mirror images to each other but have chiral centers that are not superimposable. The plasmonic analogue of diastereomers can also be constructed by stacking gold particles, where two chiral centers consisting of four gold NPs are added in a handed way (Fig. 10.5). The S-shaped first layer in the combined structures already shows two-dimensional chirality, which results in three-dimensional chiral structures regardless of the handedness. The additional gold NP placed on top of the first layer allows breaking of mirror symmetry and results in three-dimensional chirality. Interestingly, if diastereomers are weakly coupled to each other, their optical properties can be decoupled into those of two chiral centers, then added, i.e., the chiral response of the diastereomer is the sum of those of the

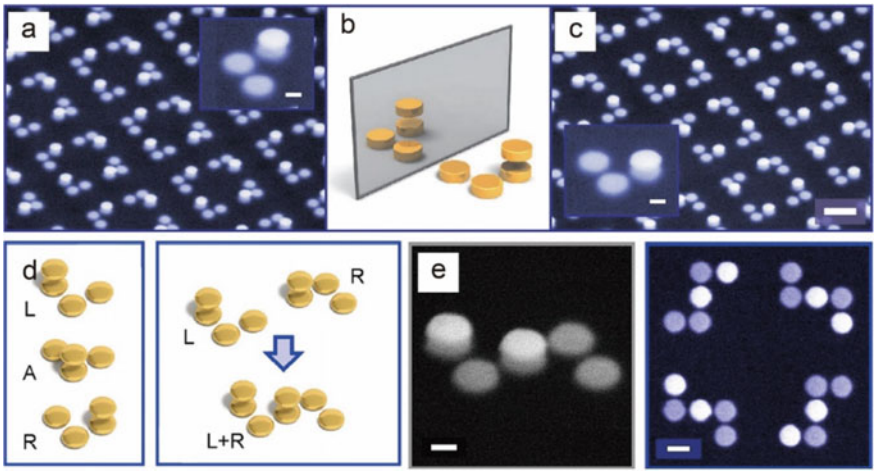

Fig. 10.5 Quadrumeric structures consisting of two layers of particles fabricated with EBL, to give chirality. The first layer consists of three particles arranged in an 'L' shape, and the second layer has one particle of which its position determines the handedness of the superstructure in a C_4 symmetric arrangement. **a**, **c** Tilted SEM images of the chiral plasmonic molecules. Scale bar: 500 nm; inset scale bar: 100 nm. **b** Schematic illustrating that the designed plasmonic molecules have chirality. **d** Process to fabricate plasmonic diastereomers. Each chiral center consists of four identical particles with three in the first and one in the second layer. As two chiral centers merge, the position of two particles in the second layer determine the chirality of the composite structure. **e** Close-up tilted and normal view of SEM images of (L+R) molecules, showing good alignment. (**a**–**c**) from [26], (**d**–**e**) from [27]

chiral centers (Fig. 10.5). However, this additivity of chiral responses does not occur if the two chiral centers are close together, and thus strongly coupled.

10.3.2 Glancing Angle Deposition

The glancing angle deposition (GLAD) method uses a bottom-up approach that is compatible with large-area fabrication, while retaining high-resolution capability down to 20 nm. The GLAD method utilizes a physical vapor deposition process with several parameters controlled, such as nanoseed pattern, substrate rotation speed and temperature. By changing these process parameters, many different shapes of 3D nanostructures can be fabricated on a large area.

Due to the nature of GLAD, the material grows as it is being rotated, and a helical nanostructure forms; this process allows easy fabrication of chiral nanostructures that operate in the visible spectrum. A typical GLAD fabrication starts with nanoseed fabrication from block copolymer micelles. The gold-loaded block copolymer is spin-coated on the wafer; subsequent plasma treatments remove the polymer to leave and array of gold dots with uniform size and spacing on the entire wafer surface. Then

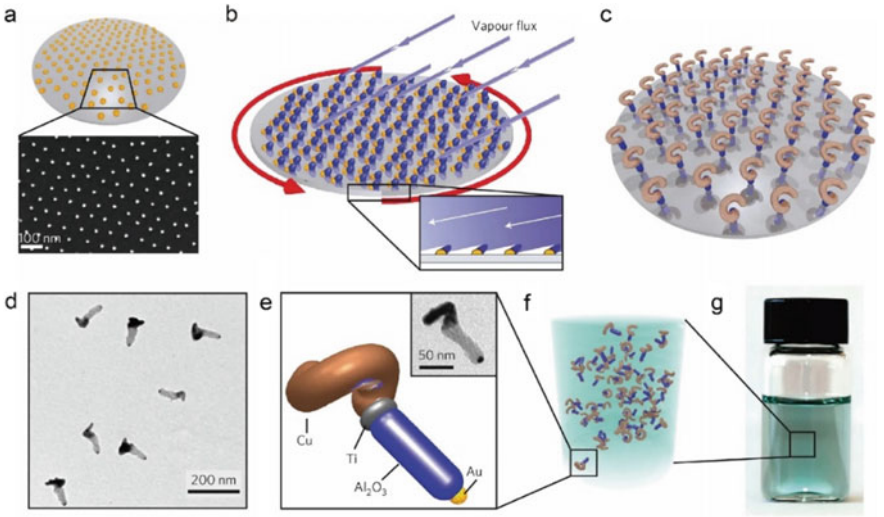

Fig. 10.6 **a** SEM image of gold nanodots regularly patterned on a wafer by micellar nanolithography. **b** Gold nanodots as nucleation sites during subsequent shadow growth. **c** Complex 3D structure can be designed on each nucleation site by manipulating the substrate angle and deposition material. **d** TEM image of hybrid insulator-metal nanohooks. **e** Schematic of the designed structure; inset: TEM image of a nanohook, suspended in a solution by using sonification. **f** Schematic and **g** photograph of the solution. (**a**–**g**) from [26]

the target material is deposited on the substrate by physical vapor deposition with grazing incidence. By manipulating the tilt angle and rotation speed of the substrate, many different kinds of nanostructures can be fabricated, including bars, zigzags and helices. Another advantage of GLAD technology is that the nanostructures made on the wafer can be removed from the substrate and immersed in a solution for use in a suspension, such suspensions in liquid may enable novel applications such as fluidic (chiral) molecular sensors and nano-robotic systems (Fig. 10.6).

Helical plasmonic NPs offer diverse set of optical response depending on thier geometrical parameters and their materials. Under irradiation, LSPR is generated along the helical axis; the strength is proportional to the total length of the helix. Therefore, nanohelices offer multiple variables for the manipulation of optical fields, including structural features such as pitch length, total number of turns, and material composition. However, fabrication of regularly shaped multi-turn helices in well-defined orientation is a difficult task.

Therefore, plasmonic helical NPs have recently been evaluated, along with advancement in fabrication techniques. Two-turn gold nanohelix structure shows a strong chiroptical response (g-factor ~0.01) in visible light [26]. The structure has 34-nm pitch and 100-nm height, which is only 1/40 as large as the similarly-shaped nanostructure fabricated by two-photon lithography, and is also smaller than the overlain structures fabricated by EBL (Fig. 10.7). To sculpt such complex helical structures and maximize their chiroptical response, requires a technique to cool them to

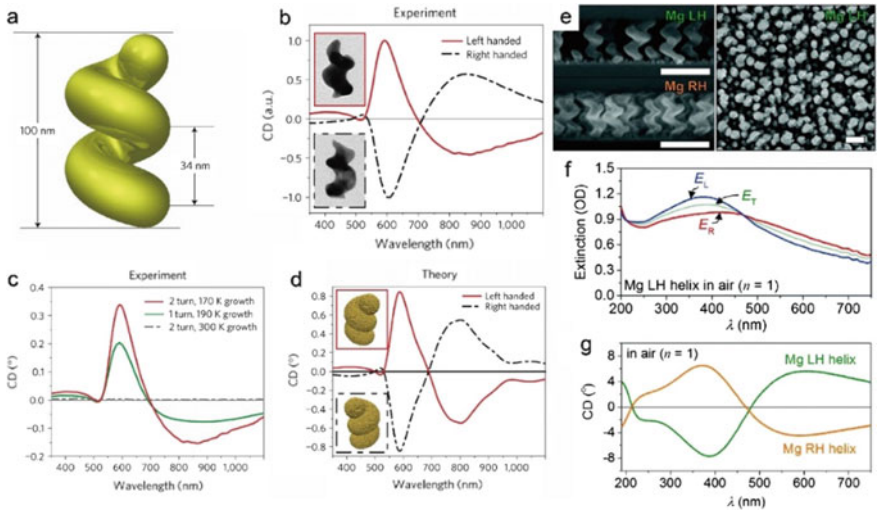

Fig. 10.7 The chiroptical response of two-turn gold nanohelix. **a** Geometrical features of the nanohelix structure. **b** Normalized circular dichroism spectra of left-handed and right-handed nanohelices; inset: TEM image of the nanohelices. **c** Circular dichroism spectra of one-turn and two-turn nanohelices grown under different cooling conditions. **d** Circular dichroism spectra simulated using a model of (**a**). The inset shows the discrete dipole model used in the simulation. **e** Side-view SEM images of left-handed (top left) and right-handed (bottom left) Mg nanohelices; scale bar: 200 nm. Right panel: top view of a left-handed array of nanohelices. **f** Extinction spectra in response to unpolarized (E_T) and circularly polarized light (E_L, E_R). **g** Circular dichroism spectra of 178-nm-thick film containing nanohelices of left or right handedness in air. (**a**–**d**) from [26], (**e**–**g**) from [29]

~170 K, particularly for materials that have high surface energy, such as noble metals. The fabricated wafer-scale helical nanostructure array (a 3 inch wafer can support roughly 10^{11} particles) can be released in the solution and can form uniform/isotropic chiral medium. The advantage of this approach is that the wavelength range in which chiral properties occur can be controlled by using an appropriate material for fabrication.

Magnesium (Mg)-based chiral NPs that work in the ultraviolet (UV) spectral range have been demonstrated [29]. Mg is widely used as a UV plasmonic material because in the UV region Mg has substantially high far-field absorption efficiency and strong near-field enhancement. Furthermore, Mg has high diffusion rate, so the Mg nanohelix structure should be sculpted in a far cooler condition ~100 K. However, Mg is highly reactive in air, so the nanohelix should be coated with a thin layer of HfO_2 or Al_2O_3 to prevent structural and chemical deformation (Fig. 10.7).

Multi-turn nickel and silver nanohelix structures show specular reflectance in the visible-and-NIR spectrum [30]. The associated optical reflectance spectrum showed minima at wavelengths that coincided with the total height of nanohelices; this result demonstrates the existence of LSPR along the axis of nanohelices. This further

confirmed that in the visible-and-NIR spectrum, the optical response was mainly dominated by the scattering from individual nanohelies (Fig. 10.7).

10.3.3 Unconventional Approaches

Chiral planar or 3D structures with chirality has merits in a way that it can have chiroptical responses. Conventional spectroscopy cannot easily detect enantiomers, because they have the same chemical and physical properties. However, CD spectroscopy can distinguish enantiomers. When they interact with circularly polarized light, the responses depend on the handedness of the molecules. This effect can be exploited to distinguish enantiomers by their chiroptical responses. However, the EM coupling of chiral molecules is typically weak, so they are commonly accompanied by plasmonic NPs. When irradiated by an EM wave of frequency that coincides with the surface plasmon frequency of the plasmonic NPs, the CD response is generated [31]. The CD response can be further improved when the coalesced plasmonic particles are also chiral; this is the motivation for creating chiral plasmonic NPs.

Single-layered chiral plasmonic NPs were demonstrated first, but such planar structures show very weak chiral response and typically require oblique incidence. Chiral interaction between light and matter is naturally increased in proportion to the propagation length of light, so a 3D structure that can offer structural variation along the incident path shows a pronounced chiroptical response.

One possible fabrication method is EBL, which can create 3D geometries with high precision. Examples include stacked gammadions, twisted crosses, and twisted layers of nanorods. However, EBL can only generate plasmonic planar and 3D structures on areas of a few square micrometers, and the method is expensive. Commercialization of chiral plasmonic NPs coupled with enantiomers requires large-area fabrication at low cost.

Hole-mask lithography (HML) combined with tilted-angle rotation evaporation has been proposed as a fabrication method (Fig. 10.8) [32]. HML is a derivative of colloidal lithography [33] that patterns surfaces with nanostructures that are created by evaporation through holes between close-packed colloidal polystyrene beads that are self-aligned throughout a thin film mask. By rotating the tilt angle through which the evaporated gold was deposited on the substrate, 3D chiral gold nanostructures can be fabricated on an area of a few square centimeters. The structure had the average outer diameter of 260 nm and structure widths from 20 to 90 nm. Rotation of the tilt angle with gradually increasing angular velocity in either positive or negative directions yielded nanostructures that had right-handed and left-handed chirality. The fabricated chiral nanostructures were illuminated with linearly polarized light in x and y directions, and with RCP and LCP lights. The transmittance spectra showed frequency modes at 150, 250, and 320 THz, which all matched simulation results.

A bilayered twisted-arc photonic metamaterial has plasmonic chiral structure that exhibits CD in the NIR spectrum (Fig. 10.8) [34]. The unit cell is composed of a pair of silver twisted arcs in different azimuthal orientation, situated on two

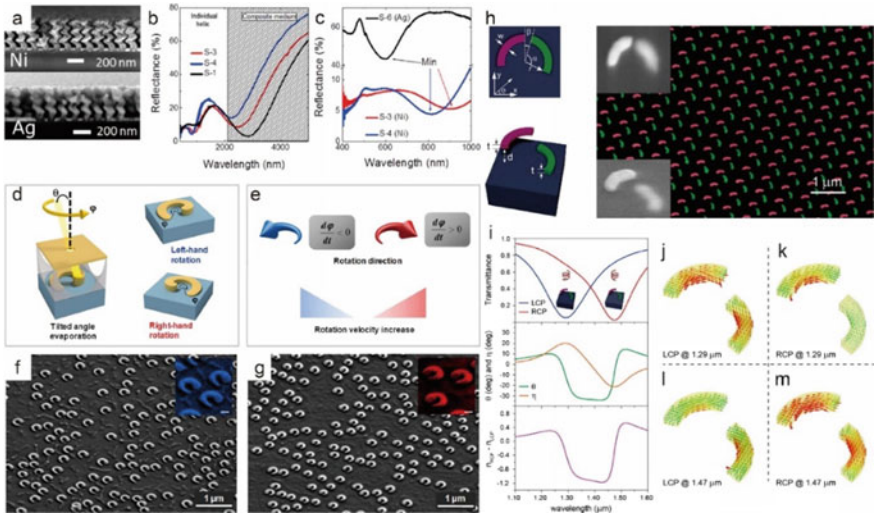

Fig. 10.8 **a** Side-view SEM images of Ni and Ag nanohelices with multiple turns. **b** Reflectance spectra of three different nanohelices at normal incidence. **c** Experimental reflectance spectra of different helices at normal incidence. **d** Hole-mask lithography combined with tilted-angle evaporation. **e** Schematic of two parameters, rotation direction and velocity, that result in 3D structure of different handedness. **f**–**g** SEM of 3D chiral structures fabricated on a large area of 1 cm^2; blue: left-handed sample; red: right-handed sample. **h** Structural geometry and SEM image of bilayered chiral metamaterial; inset: a unit cell. **i** Top: transmission spectrum. Middle: polarization rotation angle of a linearly polarized incident light and the resultant ellipticity. Bottom: difference in refractive indices for circularly polarized light of opposite handedness. **j**–**k** Induced current flow within the structure. (**a**–**c**) from [30], (**d**–**g**) from [32], (**h**–**m**) from [34]

distinct transparent layers that have given height. The unit cell is essentially a pair of planar structures, so it is fabricated using aligned EBL, in which three lithography steps are used to consecutively deposit two silver arcs separated by a transparent dielectric. The NIR transmission spectrum of LCP and RCP through the bilayered lattices agreed with full-wave simulation, with minima occurring at 1.29 μm (LCP) and 1.47 μm (RCP). The induced electric current in the dual-layered arcs generally rotated along the curved arc path and showed chiral interaction between the structure and circularly-polarized light. The plasmonic resonance modes of LCP at 1.29 μm and RCP at 1.47 μm arise by different phenomena: the induced currents collide with each other in LCP, but flow with coalescence in RCP. These features indicate that an antisymmetric mode is excited in LCP, whereas a symmetric mode is excited in RCP, and because antisymmetric resonance requires more energy than symmetric resonance, the transmission minimum is lower in LCP than in RCP.

10.4 Chirality at a Nanometer Scale: Bottom-Up Approach

Bottom-up techniques are versatile approaches to fabricate complicated nanostructures on a large scale [35–39]. These techniques have several advantages over top-down methods such as lithography and direct writing, which enable patterning of predefined structures, but can fabricate only 2D or stacked 2D structures, and are impractically expensive. On the contrary, bottom-up methods can fabricate truly-3D structures at reasonable cost. Bottom-up techniques can arrange NPs in a complex configuration with high precision and can fabricate complicated 3D geometry. They can also use diverse components including plasmonic NPs, organic materials and quantum dots. Dynamic tunability and programmability also make the bottom-up methods a powerful tool to realize 3D chiral nanostructures. In this section, we describe several such bottom-up techniques to make 3D chiral nanostructures and describe their optical characteristics.

10.4.1 Molecular Self-assembly

Molecular self-assembly is a bottom-up approach that exploits spontaneous assembly of inorganic materials such as metals, semiconductors, ceramics and biological materials including peptides, fibers and DNA [40, 41]. Synthesis from molecules in solution gives rise to plasmonic NPs that have chiral morphology. NPs that had broken mirror-symmetric geometry have been synthesized using thiolated chiral biomolecules [42]. Tellurium and selenium bind strongly with the thiol group and hence are transformed into chiral shape (Fig. 10.9a, b). Such NPs act as chiral resonators and show polarization-dependent extinction rate in the visible spectrum (Fig. 10.9c, d). The chiral tellurium nanostructures can be transformed into chiral gold and silver telluride nanostructures that have very large chiroptical activity, demonstrating a simple colloidal chemistry path to realize chiral plasmonic and semiconductor metamaterials. These materials are natural candidates for studies related to interactions of chiral biomolecules with chiral inorganic surfaces, with relevance to asymmetric catalysis, chiral crystallization and the evolution of homochirality in biomolecules.

Chiral gold NPs can be synthesized with the aid of amino acids and peptides [43–52]. During particle synthesis, amino acids and peptides interact with the particles and produce twisted high-Miller-index surfaces (Fig. 10.9e). The handedness of the input molecules determines the growth rates of chiral high-index planes that have opposite handedness. Thus, the chiral morphology of the molecules is transferred to the NPs (Fig. 10.9f). The chiral geometry of the NPs makes them interact differently with LCP and RCP. CD is significantly increased near the resonant wavelength of the gold NPs (Fig. 10.9g).

Chiroptical phenomena such as optical activity and CD do not necessarily require chiral NPs. Achiral NPs that are arranged in a chiral pattern can also exhibit an

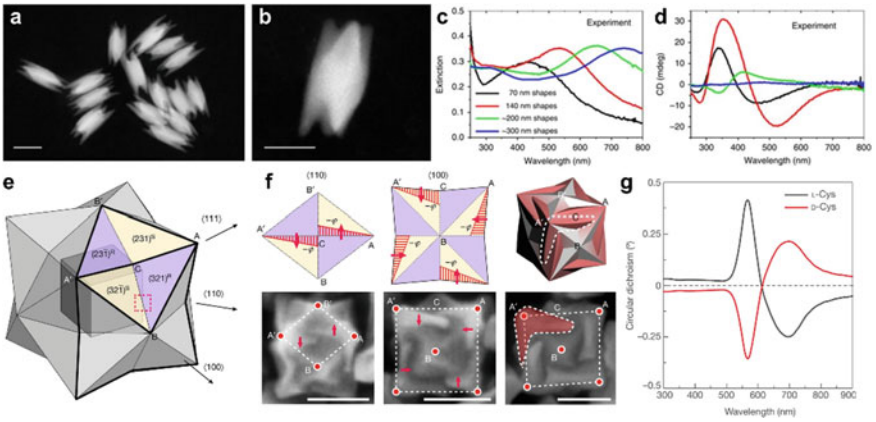

Fig. 10.9 Molecular self-assembly to produce 3D chiral nanostructures. **a**, **b** Dark-field STEM imaging of Te nanostructure with chiral shape. Experimentally-measured **c** extinction and **d** circular dichroism spectra. **e** Schematic of asymmetric growth of high-index surfaces. **f** Schematics and SEM images of chiral NPs from different view angles. **g** Circular dichroism spectra of particles synthesized using peptides that have opposite handedness. (**a**–**d**) from [42] and (**e**–**g**) from [43]

optical resonance effect as a result of inter-particle interaction [53]. Chiral assembly can be manufactured using self-organization of achiral molecules. Liquid crystals spontaneously assemble helical structures (Fig. 10.10a) that exhibit high sensitivity on plasmonic perturbation, in which handedness of the superstructure is determined by whether NIR irradiation is exposed or removed [54]. Achiral particles can also arranged in a mirror-symmetry broken pattern by using twisted fibers or layers called

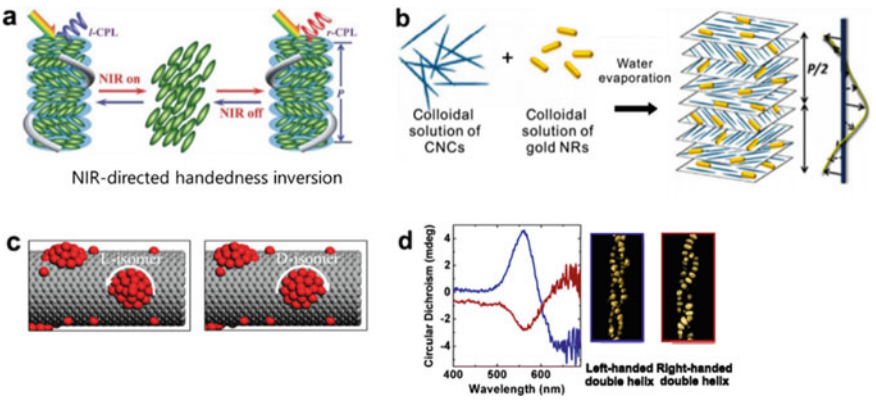

Fig. 10.10 Molecular chiral self-assembly with achiral NP. **a** Superstructures of chiral liquid crystal and their handedness differ when NIR irradiation is on or off. **b** Chiral plasmonic structures with layered CNC scaffold. **c** Assembly of gold NPs on peptide nanotube; arrows: opposite chirality. **d** Gold NP double helices based on peptide superstructures. (**a**) from [54], (**b**) from [56], (**c**) from [57], and (**d**) from [58]

scaffolds [55]. Gold nanorods load on layered twisted cellulose nanocrystal scaffolds (Fig. 10.10b) [56]. The nanoclusters that self-assemble on peptide nanotubes (Fig. 10.10c) assume either left-handed or right-handed chirality; this chiral arrangement yields CD at the surface plasmon frequency [57]. Gold NP double helices (Fig. 10.10d) are peptide-based superstructures that show plasmonic CD [58].

Molecular assembly provides a versatile route to synthesize complex 3D nanostructures, of which final morphology is determined by individual NPs and chiral symmetry groups [40]. As a result of complexity of shape, structures made by molecular assembly exhibit strong CD and chiroptical reactions. Also, the assembled plasmonic structures have no resolution limit. However, molecular assembly has some drawbacks. Control of inter-particle spacing is challenging in molecular assembly [59]. Furthermore, tuning the plasmonic coupling strength is only adjustable by particle concentration and average inter-particle range [60].

10.4.2 DNA Self-assembly

DNA, a biological molecule that is composed of double-stranded helices, can be used in self-assembly [61]. A nanotechnology that uses DNA as a building block to render 3D nanostructure is called DNA self-assembly and has unique molecular recognition capabilities. Long single-stranded DNA (ssDNA) can be folded to form a designated shape by using base pairing with short ssDNA. The long ssDNA is called the scaffold and the short ssDNA is called the staple. This fabrication technique yields 2D structure out of a 1D strand of DNA, and is often called DNA origami [62].

When NPs are functionalized with thiol-modified ssDNA, the base pairing provides 3D assembly of the NPs in a desired arrangement such as dimers [63, 64], trimers [64, 65], tetramers [66–68] and chains [69, 70]. A 3D chiral nanostructure composed of four gold NPs has been synthesized in a tetrahedral configuration by using double-stranded DNA as a scaffold to link the NPs [67]. Mirror symmetry of the tetrahedron was broken by assigning NPs with different sizes to each vertex (Fig. 10.11a). However, different sizes of the NPs and relatively large inter-particle spacing hinder efficient coupling of them, so CD was not observed.

Self-assembly of 3D chiral nanostructure can also be achieved by using a DNA template to arrange NPs in a predesignated manner. DNA origami has been used to fabricate 3D chiral nanostructures by positioning plasmonic NPs in a chiral arrangement [59]. A DNA origami bundle was used as a template to arrange gold nanospheres in a helical geometry; the nanospheres were attached to DNA strands that are complementary to the staples, which therefore attached at specified positions (Fig. 10.11b). The helically-arranged gold nanospheres yield strong CD in the visible spectrum (Fig. 10.11c). A similar structure was fabricated by rolling up a rectangular DNA sheet that had gold nanospheres attached [75]; the nanospheres were functionalized with ssDNA that was complementary with ssDNA attached to the DNA sheet. The handedness of the arrangement can be adjusted by changing the position of the

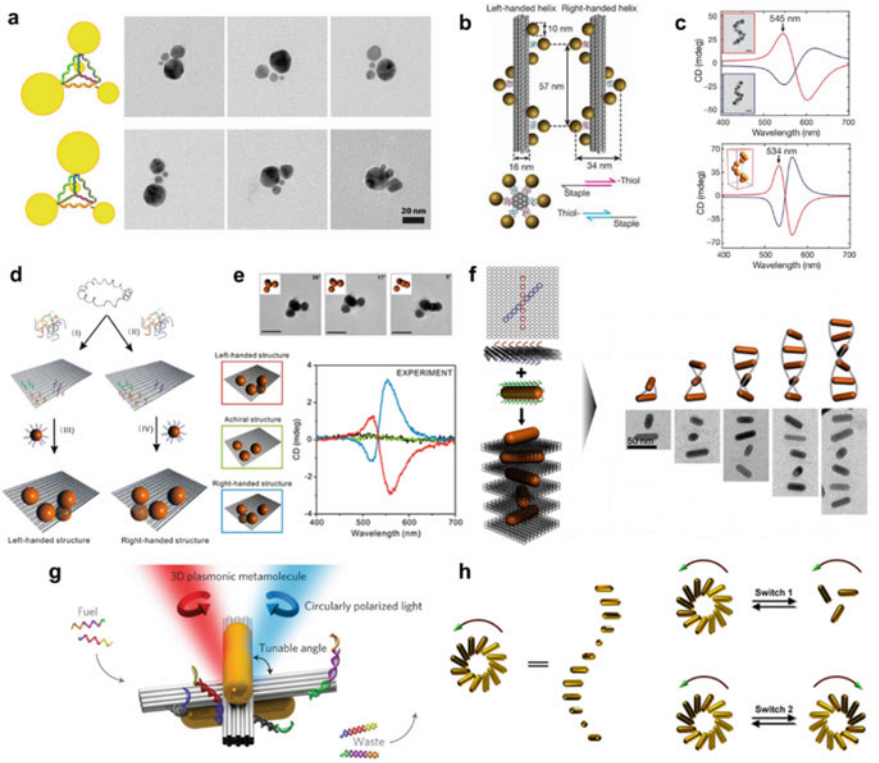

Fig. 10.11 3D chiral nanostructures synthesized by DNA self-assembly. **a** Schematics and TEM images of a tetramer of four gold NPs assembled by double-stranded DNA. **b** An assemble of gold NPs positioned by using a DNA origami bundle [59] and **c** its circular dichroism (top: measured, bottom: simulated) [59]. **d** Four gold NPs bound in a chiral arrangement by using a DNA origami sheet [71] and **e** measured circular dichroism [71]. **f** Twisted layer of gold nanorods stacked by using origami sheets [65]. **g** Schematics of a reconfigurable 3D chiral nanostructure [72]. **h** Schematics of dynamic reconfiguration. The nanorods can be switched between a tightly folded state and an extended state, and between two folded states with opposite handedness. (**a**) from [67], (**b**) and (**c**) from [59], (**d**) and (**e**) from [71], (**f**) from [73], (**g**) from [72], (**h**) from [74]

dressed nanospheres. 3D chiral nanostructures have been also made with a small number of nanospheres in a tetramer arrangement [71]; to realize a chiral geometry, four binding sites were defined on a rectangular DNA origami template, i.e., three on the top surface and one on the bottom surface (Fig. 10.11d). The position of the binding sites on the bottom surface breaks the mirror symmetry and determines the handedness. Four gold NPs were functionalized using complementary DNA strands and positioned, then one was positioned at each binding site by exploiting DNA hybridization. The fabricated structure showed CD in the visible spectrum (Fig. 10.11e).

The arrangement can be simplified by using plasmonic nanorods instead of nanospheres. A nanorod has an anisotropic geometry, which can be used as an additional degree of freedom to break mirror symmetry. Two gold nanorods oriented at 90° to each other, one on the top surface and the other on the bottom surface of the DNA origami template, were fabricated using the base-pairing mechanism [76]. The sample showed CD at $\lambda \sim 730$ nm. The CD was remarkably amplified by increasing the number of nanorods [73]. To synthesize this structure, both sides of the origami sheets were dressed with capture strands (Fig. 10.11f), which were defined in a twisted manner to achieve the chiral geometry. The twisted layer of gold nanorods had strong CD in the visible spectrum.

Tunability of chiroptical responses is an important goal. In most structures, these responses are determined by the geometrical chirality of the 3D nanostructures. Therefore, the chiroptical signal of a fabricated structure is static: its magnitude, peak wavelength and handedness cannot be changed once the structure is formed. However, DNA self-assembly facilitates programmable synthesis of particle assembles and thus provides a pathway to produce reconfigurable and multifunctional structures.

The first tunable 3D chiral nanostructure consisted of a twisted bilayer of gold nanorods [72] (Fig. 10.11g), which were attached individually to two connected origami bundles. The relative angle between two bundles and hence, the handedness of the chiral structure was dynamically controlled by two DNA locks. Here, DNA strands were used both as structural components, and as a tool to drive structural change. The fabricated sample showed CD near a $\lambda = 700$ nm, and the sign of the response could be flipped by applying external stimuli. Time-domain CD confirmed the tunable and reversible chiroptical responses. Alternatively, the distance between two nanorods, rather than the relative angle, can be adjusted to actively control chiroptical responses [77]. Two nanorods were positioned perpendicularly at opposite sides of a double-layer DNA origami. One of the nanorods walked on the surface of the sheet as a result of interacting fuel strands while the other was stationary.

Reconfigurable 3D chiral nanostructure has also been realized by folding a helical assembly of gold nanorods [74] (Fig. 10.11h), which had been positioned helically by using self-assembled DNA origami. DNA-toehold-mediated conformational changes in the DNA template enabled conversion between a tightly-folded state and an extended state, and between tightly-folded states with opposite handedness. The transformation was reversible, but the recovery efficiency is low because of the leakage of the strand-displacement reactions.

10.4.3 Block Copolymer Self-assembly

Block copolymer (BCP) self-assembly exploits phase separation and reconstruction of block copolymers to make light-matter interacting plasmonic nanostructures. A BCP consists more than one species of monomers, which are repeating units joined by covalent bonds to a organize a polymer chain. BCPs are classified according to

the number of blocks and the shape of the polymer. Segments of BCP aggregate to reach thermal equilibrium, and this process leads to spontaneous assembly of BCPs. For example, a chiral gyroid structure can be synthesized by controlling the volume fraction of each block [78]. Even though the BCPs are composed of the same species of monomer units, the final morphology of the assembled BCP after order-to-disorder transition differs depending on the interaction between segments, the volume fraction of the blocks, the polymer structures and the solution-processing routes.

Pure BCPs do not readily yield a plasmonic surface effect, so inorganic materials must be combined with them. Two synthesis strategies have been used: templating and coassembly.

Templating transfers polymer morphology into an inorganic phase by deposition after BCP self-assembly. A non-centrosymmetric thin film plasmonic nanostructure could be synthesized using a templating method with linear ABC triblock copolymer, which has two end groups with single backbone chain and three distinct blocks (Fig. 10.12). A chiral alternating gyroid network (G^A), which has chiral spirals, could be generated by manipulating the volume fraction of the block copolymer (Fig. 10.12a) [79]. After an isoprene-block-styrene-block-ethylene oxide (ISO) polymer is assembled as alternating gyroid structures on the substrate (Fig. 10.12b), one of the gyroid networks is eliminated by selective UV and chemical etching (Fig. 10.12c). The resulting space is back-filled by gold electrodeposition, then the rest of the polymer is removed by plasma etching (Fig. 10.12d) to leave a continuous

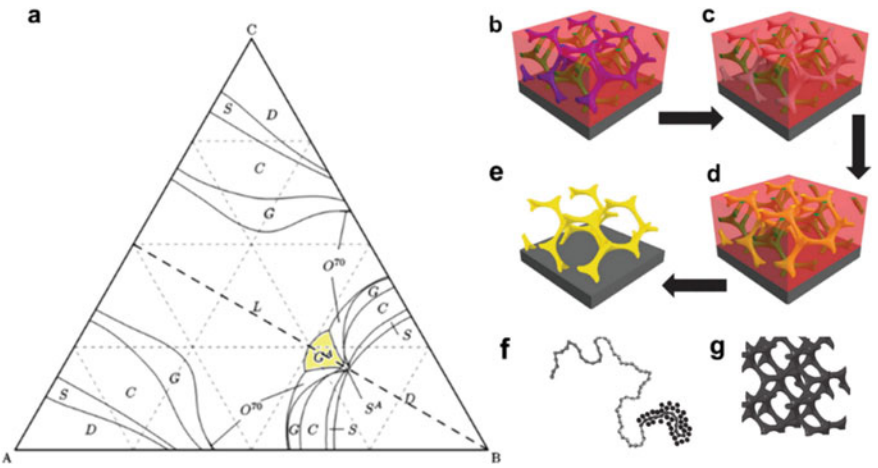

Fig. 10.12 **a** ABC triblock copolymer morphology diagram. The triblock copolymer corresponding volume fraction of G^A part self assembles as chiral alternating gyroid network. (**b–e**) BCP self-assembled chiral plasmonic structure by templating method. **b** ISO polymers assembled into alternating gyroid structures on the substrate. **c** Removing one gyroid by etching **d** Gold electrodeposition. **e** Final gyroid structure by templating. (**f–g**) BCP self-assembly chiral plasmonic structure by coassembly method. **f** Triblock poly(isoprene-b-styrene-b-ethylene oxide) and introduced sol(black particles) **g** Final gyroid structure by coassembly. (**a**) from [79], (**b–e**) from [78], and (**f–g**) from [81]

triple-periodic gold network (Fig. 10.12e) [80]. The templating approach has major disadvantages that deposited amorphous materials may crystallize, and that strain can accumulate.

Coassembly exploits intermolecular force to get an amphiphilic block copolymer to interact with inorganic materials in solution. This method has been used to fabricate an isoprene-block-styrene-block-ethylene oxide polymer with sol (black particles in Fig. 10.12f); the intermolecular forces drive the particles into the hydrophilic PEO blocks to yield an alternative gyroid structure [81] (Fig. 10.12g). The coassembly approach has disadvantages that the amorphous assemblies can shrink and crack during forming and crystallization, but it could be used to construct superlattices for novel photonic applications.

Fabrication using BCP self-assembly is a solution process and uses inexpensive constituent monomers, so it is less expensive than photolithography. Bottom up BCP self-assembly has a great advantage to fabricate sub-wavelength highly ordered nanostructures over large areas of a surface. These abilities are advantages over top-down approaches such as lithography, which have resolution limits. In addition, BCP self-assembly is much simpler sequences and requires fewer repeating units than biological molecular assembly that uses DNA or peptides [78]. BCP self-assembled plasmonic structure has been applied for organic solar cells, optoelectronics, and plasmonic nanoantennas, and can help to fabricate subminiature drug delivery systems and biosensing devices [82, 83].

10.5 Conclusion

In this chapter, fabrication methods realizing three-dimensional chiral structures were discussed and categorized by their manufacturing feature sizes since the working wavelength of enhanced artificial chirality is generally close to the feature sizes of the chiral structures. Top-down approaches can be used to fabricate micron-scale structures with high precision. Direct laser writing, focused ion beam, and photolithography can be used to realize three-dimensional structures with a large degree-of-freedom; however, they are time-consuming and expensive. Bottom-up approaches are more suitablefor realizing nano-scale structures. Solution processing and block copolymer self-assembly are cost-effective methods, but the achievable morphologies are limited.

Acknowledgements This work was financially supported by the National Research Foundation (NRF) grant (NRF-2019R1A2C3003129) funded by the Ministry of Science and ICT, Republic of Korea. Y.Y. and Y.K. acknowledge the fellowships from the Hyundai Motor *Chung Mong-Koo* Foundation. S.S., M.K. and I.K. acknowledge the NRF Global Ph.D. fellowships (NRF-2017H1A2A1043322, NRF-2017H1A2A1043204, NRF-2016H1A2A1906519), respectively, funded by the Ministry of Education, Republic of Korea.

Author Contributions J. R., Y. Y. and Y. K. conceived and initiated the project. Y. Y., Y. K. and J. M. mainly wrote the manuscript. J. G, S. S., M. K., H. J., I. K. and T. B. are partially involved in

writing the manuscript. Y. Y and J. G organized the top-down fabrication parts with support from J. G, S. S., Y. K., H. J., I. K., Y. Y. and M. K. organized bottom-up fabrication parts with support from J. M.. All authors read and approved the final manuscript. J. R. guided the entire project.

Additional Information The authors declare no competing interests.

References

1. J. Mun, M. Kim, Y. Yang, T. Badloe, J. Ni, Y. Chen, C-W. Qiu, J. Rho, Light Sci. Appl. **9**, 139 (2020)
2. P. Bharadwaj, B. Deutsch, L. Novotny, Adv. Opt. Photonics **1**, 438 (2009)
3. L. Novotny, Phys. Rev. Lett. **98**, 266802 (2007)
4. A. Campion, P. Kambhampati, Chem. Soc. Rev. **27**, 241 (1998)
5. D. Jaque, L. Martínez Maestro, B. Del Rosal, P. Haro-Gonzalez, A. Benayas, J. L. Plaza, E. Martín Rodríguez, and J. García Solé, Nanoscale **6**, 9494 (2014).
6. L. Novotny, N. Van Hulst, Nat. Photonics **5**, 83 (2011)
7. X. Fan, W. Zheng, D.J. Singh, Light Sci. Appl. **3**, e179 (2014)
8. J. Mun, S. So, J. Rho, Phys. Rev. Appl. **10**, 1 (2019)
9. J. Mun, J. Rho, Opt. Lett. **43**, 2856 (2018)
10. J.K. Gansel, M. Thiel, M.S. Rill, M. Decker, K. Bade, V. Saile, G. Von Freymann, S. Linden, M. Wegener, Science **325**, 1513 (2009)
11. A. Phys, J.K. Gansel, M. Latzel, A. Frölich, J. Kaschke, M. Thiel, Opt. Express **101109**, 19936 (2017)
12. J. Kaschke, L. Blume, L. Wu, M. Thiel, K. Bade, Z. Yang, M. Wegener, Adv. Opt. Mater. **3**, 1411 (2015)
13. Z. Wang, F. Cheng, T. Winsor, Y. Liu, Nanotechnology **27**, 412001 (2016)
14. A. Selimis, V. Mironov, M. Farsari, Microelectron. Eng. **132**, 83 (2015)
15. Z. Liu, H. Du, J. Li, L. Lu, Z.Y. Li, N.X. Fang, Sci. Adv. **4**, 1 (2018)
16. A. Rafsanjani, K. Bertoldi, Phys. Rev. Lett. **118**, 084301 (2017)
17. Z. Chen, G. Huang, I. Trase, X. Han, Y. Mei, Phys. Rev. Appl. **5**, 017001 (2016)
18. E.A. Peraza-hernandez, D.J. Hartl, R.J.M. Jr, D.C. Lagoudas, Computer-aid Design **78**, 93 (2014)
19. L. Xu, T.C. Shyu, N.A. Kotov, ACS Nano **11**, 7587 (2017)
20. S. Xu, Z. Yan, K. Jang, W. Huang, H. Fu, J. Kim, Z. Wei, M. Flavin, J. Mccracken, R. Wang, A. Badea, Y. Liu, D. Xiao, G. Zhou, J. Lee, H.U. Chung, H. Cheng, W. Ren, A. Banks, X. Li, U. Paik, R.G. Nuzzo, Y. Huang, Science **347**, 154 (2015)
21. S. Zhang, J. Zhou, Y.S. Park, J. Rho, R. Singh, S. Nam, A.K. Azad, H.T. Chen, X. Yin, A.J. Taylor, X. Zhang, Nat. Commun. **3**, 942 (2012)
22. S. Zhang, Y.-S. Park, J. Li, X. Lu, W. Zhang, X. Zhang, Phys. Rev. Lett. **102**, 23901 (2009)
23. G. Yoon, I. Kim, S. So, J. Mun, M. Kim, J. Rho, Sci. Rep. **7**, 6668 (2017)
24. Y. Zhao, M.A. Belkin, A. Alù, Nat. Commun. **3**, 870 (2012)
25. M. Hentschel, M. Schäferling, T. Weiss, N. Liu, H. Giessen, Nano Lett. **12**, 2542 (2012)
26. A.G. Mark, J.G. Gibbs, T.C. Lee, P. Fischer, Nat. Mater. **12**, 802 (2013)
27. M. Hentschel, M. Schäferling, B. Metzger, H. Giessen, Nano Lett. **13**, 600 (2013)
28. Y. Yang, M. Kim, J. Mun, J. Rho, Adv. Theory Simul. **3**, 1900229 (2020)
29. H.-H. Jeong, A.G. Mark, P. Fischer, Chem. Commun. **52**, 12179 (2016)
30. J.M. Caridad, D. McCloskey, F. Rossella, V. Bellani, J. F. Donegan, V. Krstić, ACS Photonics **2**, 675 (2015)
31. M. Kim, J. Rho, Opt. Express **26**, 14051 (2018)
32. B. Frank, X. Yin, M. Schäferling, J. Zhao, S.M. Hein, P.V. Braun, H. Giessen, ACS Nano **7**, 6321 (2013)

33. H. Fredriksson, Y. Alaverdyan, A. Dmitriev, C. Langhammer, D.S. Sutherland, M. Zäch, B. Kasemo, Adv. Mater. **19**, 4297 (2007)
34. Y. Cui, L. Kang, S. Lan, S. Rodrigues, W. Cai, Nano Lett. **14**, 1021 (2014)
35. Y.Y. Lee, R.M. Kim, S.W. Im, M. Balamurugan, K.T. Nam, Nanoscale **12**, 58 (2020)
36. A spin-encoded all-dielectric metahologram for visible light. Laser Photon. Rev. **13**, 1900065 (2019)
37. Complex-amplitude metasurface-based orbital angular momentum holography in momentum space. Nature Nanotechnol. **15**, 948–955 (2020)
38. Planar achiral metasurfaces-induced anomalous chiroptical effect of optical spin isolaton. ACS Appl. Mater. Inter. **12**, 43 (2020)
39. Multipole decomposition for interactions between structured optical fields and meta-atoms. Optic. Express **28**, 36756–36770 (2020)
40. H.-E. Lee, H.-Y. Ahn, J. Lee, K.T. Nam, ChemNanoMat **3**, 685 (2017)
41. W. Ma, L. Xu, A.F. De Moura, X. Wu, H. Kuang, C. Xu, N.A. Kotov, Chem. Rev. **117**, 8041 (2017)
42. A. Ben-Moshe, S.G. Wolf, M.B. Sadan, L. Houben, Z. Fan, A.O. Govorov, G. Markovich, Nat. Commun. **5**, 4302 (2014)
43. H.-E. Lee, H.-Y. Ahn, J. Mun, Y.Y. Lee, M. Kim, N.H. Cho, K. Chang, W.S. Kim, J. Rho, K.T. Nam, Nature **556**, 360 (2018)
44. H.-E. Lee, R.M. Kim, H.-Y. Ahn, Y.Y. Lee, G.H. Byun, S.W. Im, J. Mun, J. Rho, K.T. Nam, Nat. Commun. **11**, 263 (2020)
45. L. Ohnoutek, N.H. Cho, A.W.A. Murphy, H. Kim, D.M. Rasadean, G.D. Pantoș, K.T. Nam, V.K. Valev, Nano Lett. **8**, 5792 (2020)
46. N.H. Cho, H. Lee, H. Ahn, Y.Y. Lee, S.W. Im, H. Kim, K.T. Nam, Part. Part. Syst. Charact. **36**, 1900062 (2019)
47. J. Karst, N.H. Cho, H. Kim, H.-E. Lee, K.T. Nam, H. Giessen, M. Hentschel, ACS Nano **13**, 8659 (2019)
48. H.-Y. Ahn, S. Yoo, N.H. Cho, R.M. Kim, H. Kim, J.-H. Huh, S. Lee, K.T. Nam, Acc. Chem. Res. **52**, 2768 (2019)
49. S.W. Im, H.Y. Ahn, R.M. Kim, N.H. Cho, H. Kim, Y.C. Lim, H.E. Lee, K.T. Nam, Adv. Mater. **31**, 1905758 (2019)
50. Y.Y. Lee, N.H. Cho, S.W. Im, H. Lee, H. Ahn, K.T. Nam, Chem. Nano Mat. **6**, 362 (2020)
51. N.H. Cho, G.H. Byun, Y.-C. Lim, S.W. Im, H. Kim, H.-E. Lee, H.-Y. Ahn, K.T. Nam, ACS Nano **14**, 3595 (2020)
52. H. Kim, S.W. Im, N.H. Cho, D. Hye Seo, R. M. Kim, Y. Lim, H. Lee, H. Ahn, K.T. Nam, Angew. Chemie. **59**, 12976 (2020)
53. J. Mun, J. Rho, Nanophotonics **8**, 941 (2019)
54. L. Wang, K.G. Gutierrez-Cuevas, A. Urbas, Q. Li, Adv. Opt. Mater. **4**, 247 (2016)
55. A. Guerrero-Martínez, B. Auguié, J.L. Alonso-Gómez, Z. Džolić, S. Gómez-Graña, M. Žinić, M.M. Cid, L.M. Liz-Marzán, Angew. Chemie Int. Ed. **50**, 5499 (2011)
56. M. Hentschel, M. Schäferling, X. Duan, H. Giessen, N. Liu, Sci. Adv. **3**, e1602735 (2017)
57. J. George, K.G. Thomas, J. Am. Chem. Soc. **132**, 2502 (2010)
58. C. Song, M.G. Blaber, G. Zhao, P. Zhang, H.C. Fry, G.C. Schatz, N.L. Rosi, Nano Lett. **13**, 3256 (2013)
59. A. Kuzyk, R. Schreiber, Z. Fan, G. Pardatscher, E.-M. Roller, A. Högele, F.C. Simmel, A.O. Govorov, T. Liedl, Nature **483**, 311 (2012)
60. W. Ma, H. Kuang, L. Wang, L. Xu, W.-S. Chang, H. Zhang, M. Sun, Y. Zhu, Y. Zhao, L. Liu, Sci. Rep. **3**, 1934 (2013)
61. N.C. Seeman, J. Theor. Biol. **99**, 237 (1982)
62. P.W.K. Rothemund, Nature **440**, 297 (2006)
63. A.P. Alivisatos, K.P. Johnsson, X. Peng, T.E. Wilson, C.J. Loweth, M.P. Bruchez, P.G. Schultz, Nature **382**, 609 (1996)
64. K.L. Wustholz, A.-I. Henry, J.M. McMahon, R.G. Freeman, N. Valley, M.E. Piotti, M.J. Natan, G.C. Schatz, R.P. Van Duyne, J. Am. Chem. Soc. **132**, 10903 (2010)

65. C.J. Loweth, W.B. Caldwell, X. Peng, A.P. Alivisatos, P.G. Schultz, Angew. Chemie Int. Ed. **38**, 1808 (1999)
66. A. Fu, C.M. Micheel, J. Cha, H. Chang, H. Yang, A.P. Alivisatos, J. Am. Chem. Soc. **126**, 10832 (2004)
67. A.J. Mastroianni, S.A. Claridge, A.P. Alivisatos, J. Am. Chem. Soc. **131**, 8455 (2009)
68. W. Chen, A. Bian, A. Agarwal, L. Liu, H. Shen, L. Wang, C. Xu, N.A. Kotov, Nano Lett. **9**, 2153 (2009)
69. Z. Deng, Y. Tian, S.-H. Lee, A.E. Ribbe, C. Mao, Angew. Chemie Int. Ed. **44**, 3582 (2005)
70. S. Beyer, P. Nickels, F.C. Simmel, Nano Lett. **5**, 719 (2005)
71. X. Shen, A. Asenjo-Garcia, Q. Liu, Q. Jiang, F.J. García de Abajo, N. Liu, B. Ding, Nano Lett. **13**, 2128 (2013)
72. A. Kuzyk, R. Schreiber, H. Zhang, A.O. Govorov, T. Liedl, N. Liu, Nat. Mater. **13**, 862 (2014)
73. X. Lan, X. Lu, C. Shen, Y. Ke, W. Ni, Q. Wang, J. Am. Chem. Soc. **137**, 457 (2014)
74. X. Lan, T. Liu, Z. Wang, A.O. Govorov, H. Yan, Y. Liu, J. Am. Chem. Soc. **140**, 11763 (2018)
75. X. Shen, C. Song, J. Wang, D. Shi, Z. Wang, N. Liu, B. Ding, J. Am. Chem. Soc. **134**, 146 (2012)
76. X. Shen, P. Zhan, A. Kuzyk, Q. Liu, A. Asenjo-Garcia, H. Zhang, F.J. García de Abajo, A. Govorov, B. Ding, N. Liu, Nanoscale **6**, 2077 (2014)
77. C. Zhou, X. Duan, N. Liu, Nat. Commun. **6**, 8102 (2015)
78. M. Stefik, S. Guldin, S. Vignolini, U. Wiesner, U. Steiner, Chem. Soc. Rev. **44**, 5076 (2015)
79. C.A. Tyler, J. Qin, F.S. Bates, D.C. Morse, Macromolecules **40**, 4654 (2007)
80. S. Vignolini, N. A. Yufa, P. S. Cunha, S. Guldin, I. Rushkin, M. Stefik, K. Hur, U. Wiesner, J. J. Baumberg, U. Steiner, Adv. Mater. **24**, OP23 (2012)
81. P. Docampo, M. Stefik, S. Guldin, R. Gunning, N.A. Yufa, N. Cai, P. Wang, U. Steiner, U. Wiesner, H.J. Snaith, Adv. Energy Mater. **2**, 676 (2012)
82. S.J. Go, D.-E. Lee, D.H. Lee, B.D. Chin, J. Korean Phys. Soc. **68**, 257 (2016)
83. I. Jung, M. Kim, M. Kwak, G. Kim, M. Jang, S.M. Kim, D.J. Park, S. Park, Nat. Commun. **9**, 1010 (2018)